19th AIAA Computational Fluid Dynamics
22 - 25 June 2009, San Antonio, Texas

AIAA 2009-3891

Application of an AMR strategy to an abstract bubble vibration model

Yohan PENEL*, Anouar MEKKAS†, Stéphane DELLACHERIE†
Commissariat à l'Énergie Atomique (CEA), Centre de Saclay
DEN/DANS/DM2S/SFME, 91191 Gif-sur-Yvette, France.

Juliet RYAN‡ , Michel BORREL‡
Office National d'Études et de Recherches Aérospatiales (ONERA)
BP 72, 92322 Châtillon cedex, France.

We describe in this paper the improvement on the numerical resolution of a fluid dynamics system by means of an Adaptive Mesh Refinement algorithm in order to handle an infinitely thin interface. This model is derived from the compressible Navier-Stokes equations in the case of diphasic flows for which both phases have a low Mach number. It consists of a coupled hyperbolic-elliptic system. The first part is numerically treated thanks to a hierarchical grid structure whereas we use the Local Defect Correction method to solve the second part.

I. Introduction

In the framework of safety evaluations for nuclear reactors, we are interested in studying the evolution of gas bubbles in a liquid phase. Indeed, in Pressurized Water Reactor (PWR) or in Boiling Water Reactor (BWR), a vapor phase may appear in the liquid phase. As progress in Computer Science over the past decades enables us to take into account a large range of spatial scales from the mesoscopic one (bubble scale) to the macroscopic one (reactor scale), it makes possible further use of Direct Numerical Simulation (DNS) and thus the numerical treatment of fine safety evaluations.

The main difficulty in this kind of problems is the modeling of the interface deformation. There exists several methods to handle such issues among which we choose an interface-capturing type algorithm. It consists in representating implicitly the discontinuity by means of the resolution of a transport equation of a discontinuous marker function (*via* an antidiffusive scheme) instead of reconstructing explicitly the interface. This transported function is a color function, namely the mass fraction of one phase, that indicates whether this phase is present or not.

As for the global system including velocity, density and energy behaviors, we derive a set of equations from the compressible diphasic Navier-Stokes equations through a formal asymptotic expansion under physical then nonphysical hypotheses: these assumptions concerned the density variable, the common properties of the two fluids and finally a potential characteristic of the velocity. The last step is then a modification of the right-hand-side of one of the equations that makes the thermodynamic variables evolution uncoupled from the velocity equation. This boils down to studying the coupling between a transport equation with a Poisson-like one. Even if this system of Partial Differential Equations (PDEs) is lacking in physical sense, its mathematical properties are useful to study the real physical system from both theoretical and numerical points of view. Despite a brief explanation about the derivation of the model, we will focus mainly on numerical aspects in this article.

*Graduate Student. yohan.penel@cea.fr (+33 1 69 08 69 86). And also: Laboratoire d'Analyse, Géométrie et Applications (LAGA), Université Paris 13, 93430 Villetaneuse, France.
†stephane.dellacherie@cea.fr (+33 1 69 08 98 11), mekkas@bertin.fr.
‡juliette.ryan@onera.fr (+33 1 46 73 44 34), michel.borrel@onera.fr (+33 1 46 73 42 83).

The fact still remains that most variables are discontinuous through the interface. That is why a refinement strategy turns out to be useful. However, instead of refining everywhere (computationally costly), our algorithm is based on Adaptive Mesh Refinement (AMR) techniques applied close to the discontinuity of the solution of the transport equation. As regards to the elliptic equation governing the potential velocity field, we use the Local Defect Correction (LDC) method.

II. From Navier-Stokes to an abstract bubble vibration model

We consider in our model a single set of equations governing the evolution of both phases. The Navier-Stokes equations for a compressible diphasic flow under gravity read in a conservative form:

$$\partial_t(\rho Y_1) + \nabla\cdot(\rho Y_1 \boldsymbol{u}) = 0\,, \tag{1a}$$
$$\partial_t\rho + \nabla\cdot(\rho\boldsymbol{u}) = 0\,, \tag{1b}$$
$$\partial_t(\rho\boldsymbol{u}) + \nabla\cdot(\rho\boldsymbol{u}\otimes\boldsymbol{u}) = -\nabla P + \nabla\cdot\boldsymbol{\sigma} + \rho\boldsymbol{g}\,, \tag{1c}$$
$$\partial_t(\rho E) + \nabla\cdot(\rho\boldsymbol{u}E) = -\nabla\cdot(P\boldsymbol{u}) + \nabla\cdot(\kappa\nabla T) + \nabla\cdot(\boldsymbol{\sigma}\boldsymbol{u}) + \rho\boldsymbol{g}\cdot\boldsymbol{u}\,. \tag{1d}$$

We consider System (1) in a bounded open set $\Omega\subset\mathbb{R}^d$, $d\in\{2,3\}$. The notations are standard: ρ, $\boldsymbol{u}$, $\boldsymbol{\sigma}$, P, T, E, κ and $\boldsymbol{g}$ denote respectively density, velocity field, Cauchy stress tensor, pressure, temperature, energy, thermal conductivity and gravity field. We use the classical nabla notation ∇ for all spatial differential operators (gradient, divergence). Y_1 is the mass fraction of Fluid 1 that corresponds to the characteristic function of the domain $\Omega_1(t)$ occupied by Fluid 1. If Fluid 1 occupies initially a domain $\Omega_1(0)\subset\Omega$, the initial condition associated to Eq. (1a) is:

$$Y_1(0,\boldsymbol{x}) = \mathbf{1}_{\Omega_1(0)}(\boldsymbol{x}) = \begin{cases} 1, & \text{if } \boldsymbol{x}\in\Omega_1(0),\\ 0, & \text{otherwise.}\end{cases} \tag{2}$$

We denote by $\Omega_2(t)$ the domain occupied by Fluid 2, i.e. $\Omega_2(t)=\Omega\backslash\Omega_1(t)$, and by $\Sigma(t)=\overline{\Omega}_1(t)\cap\overline{\Omega}_2(t)$ the discontinuity surface of Y_1. Capturing the interface evolution is equivalent to solving Eqs. (1a)–(2) and thus determining $\Omega_1(t)$ for all $t>0$.

Under linear elasticity hypothesis, the Cauchy stress tensor writes:

$$\boldsymbol{\sigma} = \mu(\nabla\boldsymbol{u} + {}^t\nabla\boldsymbol{u}) + \lambda(\nabla\cdot\boldsymbol{u})\,\mathcal{I}d \tag{3}$$

where μ and λ are Lamé coefficients.

As we use a single system for both phases, any state variable ξ on the whole domain is a convex combination of its values in each subdomain, that is:

$$\xi = Y_1\xi_1 + (1-Y_1)\xi_2 \tag{4}$$

where ξ_i is the corresponding value of variable ξ in the domain $\Omega_i(t)$. We finally add to System (1) boundary conditions on $\partial\Omega$

$$\boldsymbol{u} \overset{\partial\Omega}{=} 0\,, \tag{5a}$$
$$\nabla T\cdot\boldsymbol{n} \overset{\partial\Omega}{=} 0 \tag{5b}$$

as well as interface continuity conditions (where $\mathcal{I}$ is the identity tensor)

$$\begin{cases} \boldsymbol{u}_{|\Omega_1(t)} \overset{\Sigma(t)}{=} \boldsymbol{u}_{|\Omega_2(t)}\,,\\ [\boldsymbol{\sigma}-P\mathcal{I}]\,\boldsymbol{n}_{|\Omega_1(t)} \overset{\Sigma(t)}{=} [\boldsymbol{\sigma}-P\mathcal{I}]\,\boldsymbol{n}_{|\Omega_2(t)}\,,\\ T_{|\Omega_1(t)} \overset{\Sigma(t)}{=} T_{|\Omega_2(t)}\,,\\ \kappa_1\nabla T\cdot\boldsymbol{n}_{|\Omega_1(t)} \overset{\Sigma(t)}{=} \kappa_2\nabla T\cdot\boldsymbol{n}_{|\Omega_2(t)}\,. \end{cases} \tag{5c}$$

What follows is an adaptation to diphasic flows of earlier works about low Mach Number combustion systems of Majda and Embid.[10] Concepts and techniques are applied to Eqs. (1–5) in order to obtain a low Mach number system simulating bubble behaviors in nuclear reactors.[6,7]

We assume on the one hand that ρ is a positive smooth function of $(t, \boldsymbol{x})$ and on the other hand that both fluids have common characteristic values such as Reynolds or Mach Numbers ($\mathcal{R}e_*$, $\mathcal{M}_*$).

Moreover, we suppose that we have a low Mach number flow, that reads $\mathcal{M}_* \ll 1$. Hence we can make a formal asymptotic expansion:

$$\xi(t, \boldsymbol{x}) = \xi^{(0)}(t, \boldsymbol{x}) + \mathcal{M}_*^2 \cdot \xi^{(1)}(t, \boldsymbol{x}; \mathcal{M}_*) + o(\mathcal{M}_*^2). \tag{6}$$

We insert that expansion in the nondimensioned nonconservative system derived from Eq. (1) and we use the Hodge decomposition[a] to obtain the following dimensioned Diphasic Low Mach Number (DLMN) system at order 0:

$$D_t Y_1 = 0\,, \tag{7a}$$
$$\nabla \cdot \boldsymbol{u} = \mathcal{G}\,, \tag{7b}$$
$$\rho D_t \boldsymbol{u} = -\nabla \Pi + \nabla \cdot \left[\mu \left(\nabla \boldsymbol{u} + {}^t\nabla \boldsymbol{u}\right)\right] + \rho \boldsymbol{g}\,, \tag{7c}$$
$$\rho c_p D_t T = \alpha T P'(t) + \nabla \cdot (\kappa \nabla T)\,, \tag{7d}$$

where we introduce some standard thermodynamic notations:

- $\alpha = -\dfrac{1}{\rho}\left(\dfrac{\partial \rho}{\partial T}\right)_P$ is the compressibility coefficient;
- $c_p = \left(\dfrac{\partial \varepsilon}{\partial T}\right)_P + \dfrac{\alpha P}{\rho}$ is the heat capacity at constant pressure; ε is the internal energy;
- $D_t = \partial_t + (\boldsymbol{u} \cdot \nabla)$ is the material derivative;
- $-\nabla\Pi$ is the Hodge projection upon the gradient field of $\rho D_t \boldsymbol{u} - \rho \boldsymbol{g} - \nabla \cdot \left[\mu \left(\nabla \boldsymbol{u} + {}^t\nabla \boldsymbol{u}\right)\right]$; Π can be interpreted as a dynamic pressure whereas P is the thermodynamic pressure. As detailed in Refs. 6,10, the pressure variable P is spatially homogeneous owing to the singularity in $\mathcal{M}_*$;
- equation (1b) is rewritten under the form $\nabla \cdot \boldsymbol{u} = \mathcal{G}$ so as to underline the compressibility of the fluids. Function $\mathcal{G}$ can be expressed as follows:

$$\mathcal{G} = -\frac{D_t \rho}{\rho} = -\frac{1}{\Gamma}\frac{P'(t)}{P(t)} + \frac{\beta \nabla \cdot (\kappa \nabla T)}{P(t)}. \tag{7e}$$

  We introduced here the nondimensioned coefficient $\beta = \dfrac{\alpha P}{\rho c_p}$ as well as the sound velocity c deduced from $\dfrac{1}{c^2} = \left(\dfrac{\partial \rho}{\partial P}\right)_T - \dfrac{\alpha^2 T}{c_p}$ in order to define $\Gamma = \dfrac{\rho c^2}{P}$.

We finally assume that the velocity is potential, i.e. that there exists a potential ϕ such that $\boldsymbol{u} = \nabla\phi$. This is equivalent to assuming that the free-divergence part of $\boldsymbol{u}$ is zero. System (7) thus amounts to:

$$D_t Y_1 = 0\,, \tag{8a}$$
$$\Delta \phi = \mathcal{G}\,, \tag{8b}$$
$$\rho c_p D_t T = \alpha T P'(t) + \nabla \cdot (\kappa \nabla T) \tag{8c}$$

together with initial condition (2) and boundary conditions:

$$\nabla\phi \cdot \boldsymbol{n} \overset{\partial\Omega}{=} 0\,, \tag{8d}$$
$$\nabla T \cdot \boldsymbol{n} \overset{\partial\Omega}{=} 0\,. \tag{8e}$$

[a] Each field $\boldsymbol{u} \in \left(L^2(\Omega)\right)^2$ writes as the sum of a gradient field and a free-divergence one: there exists $(\phi, \boldsymbol{w}) \in H^1(\Omega) \times \left(L^2(\Omega)\right)^2$ such that $\nabla \cdot \boldsymbol{w} = 0$, $\boldsymbol{w} \cdot \boldsymbol{n}_{|\partial\Omega} = 0$ and $\boldsymbol{u} = \nabla\phi + \boldsymbol{w}$.

This system – that we name potential-DLMN system – is numerically simulated in Ref. 7 without AMR. Let us make a few comments on System (8). First, whereas Eq. (7b) was a vector second-order PDE with respect to $\boldsymbol{u}$, System (8) becomes a scalar second-order PDE with respect to ϕ. The latter system does not require the strong boundary condition (5a) anymore. That is why we just impose the Neumann boundary condition (8d) for ϕ. Secondly, we recall that there exists a unique solution (up to an additive constant) to Eqs. (8b)–(8d) provided that:[b]

$$\int_\Omega \mathcal{G}(t,\boldsymbol{x})\,d\boldsymbol{x} = 0. \tag{9}$$

Given Eq. (7e), the necessary and sufficient condition (9) is equivalent to the integro-differential equation for P:

$$P'(t) = \frac{\displaystyle\int_\Omega \beta(Y_1,T,P)\nabla\cdot(\kappa\nabla T)\,d\boldsymbol{x}}{\displaystyle\int_\Omega \frac{1}{\Gamma(Y_1,T,P)}\,d\boldsymbol{x}}. \tag{10}$$

The notations $\beta(Y_1,T,P)$ and $\Gamma(Y_1,T,P)$ mean that β and Γ depend on the set of variables (Y_1,T,P) we decided to work with but are not necessarily explicit functions. Moreover, we should bear in mind that the right-hand-side $\mathcal{G}$ of the Laplace equation also depends on the same variables, which implies a coupling between Eqs. (8a–8c)-(10). In order to analyze theoretically and numerically the coupled hyperbolic-elliptic structure of Eqs. (8a)–(8b) independently from Eqs. (8c)-(10), we modify $\mathcal{G}$ so that it does not depend on T and P anymore. A simple model of functional of variable Y_1 that satisfies the condition (9) is the projection $\mathcal{P}$ on the space of zero mean-value functions. Thus, we get interested in studying the following system called Abstract Bubble Vibration (ABV) model:

$$\partial_t Y_1 + \nabla\phi\cdot\nabla Y_1 \overset{\Omega}{=} 0\,, \tag{11a}$$

$$\Delta\phi \overset{\Omega}{=} \psi(t)\mathcal{P}(Y_1)\,, \tag{11b}$$

$$Y_1(0,\boldsymbol{x}) \overset{\Omega}{=} Y^0(\boldsymbol{x})\,, \tag{11c}$$

$$\nabla\phi\cdot\boldsymbol{n} \overset{\partial\Omega}{=} 0 \tag{11d}$$

with $\mathcal{P}$ given by:

$$\mathcal{P}(Y_1) = Y_1(t,\boldsymbol{x}) - \frac{1}{|\Omega|}\int_\Omega Y_1(t,\boldsymbol{x}')\,d\boldsymbol{x}'. \tag{11e}$$

The function ψ is a given smooth function on $(0,+\infty)$ that is considered as a pulse and Y^0 is given by Eq. (2).

The change of right-hand-side results in the absence of thermodynamic effects. Although this system has thus no longer physical sense, it is important for its mathematical structure. It also enables us to validate our interface-capturing algorithm. Indeed, under a smoothness hypothesis on Y^0, there exists a unique solution of System (11) in a Sobolev-type functional space (see Ref. 8). This is an important result for the more general study of System (7). Otherwise, if Y^0 is the nonsmooth function given by Eq. (2) and if $Y_1(t,\boldsymbol{x}) = \mathbf{1}_{\Omega_1(t)}(\boldsymbol{x})$ is a solution of System (11), we have an explicit expression of the volume $|\Omega_1(t)|$ (see Lemma 1.1, Ref. 8):

$$|\Omega_1(t)| = |\Omega| \times \frac{C^0\exp\displaystyle\int_0^t \psi(\tau)\,d\tau}{1 + C^0\exp\displaystyle\int_0^t \psi(\tau)\,d\tau}, \qquad C^0 = \frac{|\Omega_1(0)|}{|\Omega| - |\Omega_1(0)|}. \tag{12}$$

This result provides a criterion so as to check the robustness and the efficiency of our algorithm that is based on the Després-Lagoutière antidiffusive scheme[9,13] applied to the transport equation (11a). This first-order scheme is equivalent to the UltraBee scheme in spite of a different formulation. It consists in mixing main advantages of downwind (nondiffusive) and upwind (stable) schemes. One of its main properties is a uniform control over numerical error on a few cells. This property guarantees that the transported interface remains as sharp as possible.

[b] See Ref. 5 for instance.

III. AMR strategy

Our goal in this section is to solve numerically the set of coupled PDEs (11). Although the Després-Lagoutière algorithm captures interfaces with a diffusion control, situations occur where it may become inefficient. For instance, the fluid characteristic length may become smaller than the grid size or the distance between two interfaces may decrease too much. Thus, to improve both accuracy and efficiency, we would like to increase the number of nodes but to avoid adding unrelevant points. That is why we refine grids locally close to interfaces in order to reduce computational costs and to keep the interface sharpness. Morever, given that these interfaces may evolve in time, the refinement must adapt to the solution at each time step. Considering all these remarks and taking into account the nature of the two PDEs, we adopt two different strategies to solve hyperbolic and elliptic parts, that are an AMR technique to capture accurately the interface (Eqs. 11a-11c) and the LDC method to solve the steady Laplacian operator (Eq. 11b-11d).

A. Hyperbolic part

This choice raises several issues such as selection of relevant regions to be refined, way of refining the latter or interactions between coarse and fine grids. Those points are treated in the AMR techniques developped in Refs. 2, 3, 12, 14, 16.

1. Theory

We consider in this section a transport equation with a prescribed velocity field $\boldsymbol{v}$:

$$\partial_t Y + \boldsymbol{v} \cdot \nabla Y = 0. \tag{13}$$

We would like to solve Eq. (13) on a rectangular 2D-Cartesian grid of size $N = n_x \times n_y$ with grids cells $(M_i)_{1 \leqslant i \leqslant N}$. Let $G_0 = \bigcup_{1 \leqslant i \leqslant N} M_i$ be the coarsest level grid. Unknowns are located at centers of cells.
AMR-type methods generally consist in:

1. tagging grid regions that need a higher resolution owing to large variations of the solution;
2. clustering the tagged cells into subgrids called patches;
3. refining patches according to fixed ratios.

Step 1 is realized thanks to a criterion called *sensor* and a user-tuned threshold ε. Here, we tag cell M_i if

$$\frac{|(\nabla_x Y)_i| + \left|(\nabla_y Y)_i\right|}{\max\limits_{n,m} \left[|(\nabla_x Y)_n| + |(\nabla_y Y)_m|\right]} > \varepsilon \tag{14}$$

where $(\nabla_x \cdot)_i$ and $(\nabla_y \cdot)_i$ denote discrete gradients along x and y directions in cell M_i. As for Step 2, we use the *Grouping-Clustering* algorithm introduced in Ref. 4 except we do not allow overlapping patches. In refinement methods, we must keep in mind that there should be a balance between the two following requirements:

- there should be as few patches as possible to reduce computational costs;
- patches should be as small as possible to avoid unnecessary refined area.

We denote by $(G_l)_{0 \leqslant l \leqslant L_{max}}$ successive levels of refinement called *patchworks* and by $(G_l^k)_{1 \leqslant k \leqslant K_l}$ patches of the same level l of refinement. The *grouping-clustering* algorithm is based on a hierarchical grid structure that has a *Properly Nested* property[14] (see Figure 1):

1. Successive refined patchworks are imbedded in coarser ones: $G_{L_{max}} \subset \ldots \subset G_l \subset \ldots \subset G_0$;
2. Patches of the same refinement level do not overlap: $\forall\, l \in [\![0, L_{max}]\!], \forall\, (i,j) \in [\![1, K_l]\!]^2,\ G_l^i \cap G_l^j = \emptyset$;
3. Adjacent cells to G_l must belong to G_{l-1}. This last requirement guarantees that there always exists some cells in G_{l-1} that separate G_l from $G_{l-2} \backslash G_{l-1}$.

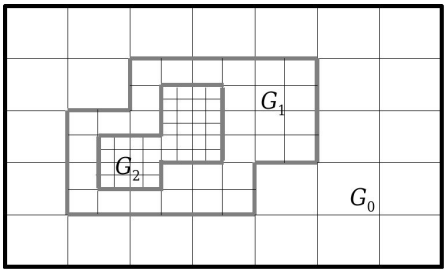

Figure 1. Example of a hierarchical grid structure satisfying the *Properly Nested* property.

We also mention that this algorithm includes the use of additional cells to handle boundary conditions: in order to prevent interfaces from crossing patchworks boundaries, we extend patches to one or more cells around them, the number of necessary cells being prescribed by the numerical scheme, e.g. 2 for the Després-Lagoutière scheme.

2. Implementation

The core of this method is based on integrations on the coarse grid then on finer grid patches in order to increase accuracy. However, those computations should interact with each other through boundary conditions (BC) which can be of different types. First, we have to compute connexions between subgrids and then to apply adapted BC. Connexions can characterize:

- ✏ physical conditions when the subgrid has common points with $\partial\Omega$. There is nothing else to do but using explicit boundary data;
- ✏ fine-fine interfaces when ghost cells associated to a given patch belong to another patch at the same level of refinement. In this case, we use values at the center of ghost cells to impose BC;
- ✏ coarse-fine interfaces when ghost cells belong to another level of refinement, whether it be finer or coarser. We use interpolations to determine BC.

For sake of simplicity, we just detail in Figure 2 the successive steps from time n to $n+1$ to solve Eq. (13) when there is only one level of refinement. G_0 is the coarse grid and $G_{1,n}$ is the evolving fine grid at time n. Function $Y^n_{G_\alpha}$ is the numerical solution at time n on grid G_α. The solver S_α is the Després-Lagoutière scheme used on G_α to solve transport equation (13). More precisely:

① Steps 1 and 1' correspond to the application of solvers $S_{1,n}$ and S_0 resp. and are computed simultaneously;

② We project $Y^{n+1}_{G_{1,n}}$ on G_0 applying the restriction operator R_0^{n+1}: we average fine grid values in each coarser cell;

As for Step 2', simultaneously to Step 2, we only keep values of $\overline{Y}^{n+1}_{G_0}$ at mesh cells that belong to G_0 but do not intersect $G_{1,n}$;

③ We gather values of the coarse and fine solutions at time $n+1$ to recover Y^{n+1} on G_0;

④ We construct the new fine grid $G_{1,n+1}$ judging from the selected nodes *via* Criterion (14) and the new coarse solution $Y^{n+1}_{G_0}$;

⑤ Given $G_{1,n+1}$ and $Y^{n+1}_{G_0}$, the projection step consists in interpolating the latter solution at new grid points;

⑥ Even if the fine mesh may evolve from time n to $n+1$, it is likely to occur that some points belong to both old and new fine grids. In that case, we recopy old fine solution values $\left(Y^{n+1}_{G_{1,n}}\right)$ at those points and new values $\left(\overline{Y}^{n+1}_{G_{1,n+1}}\right)$ at others. The corresponding operator is called U_n^{n+1}.

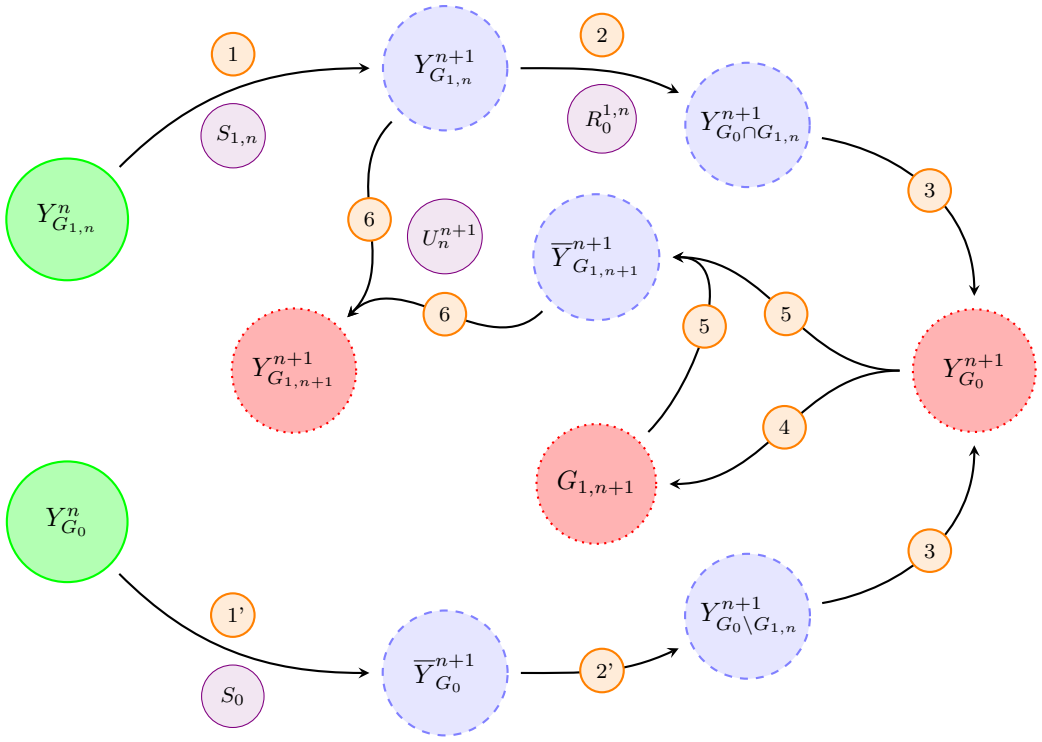

Figure 2. Scheme from time n to $n+1$. Green (plain), Blue (dashed), and Red (dots) bubbles are respectively data at time n, intermediate calculated values, and required data at time $n+1$. Close to arrows, Violet (thin) and Orange (thick) bubbles correspond to operators and successive steps.

We should bear in mind that both solutions $Y^n_{G_0}$ et $Y^n_{G_{1,n}}$ may have components 1 or 0. Thus, projection steps ② and ⑤ may induce numerical errors. In case there are common new and old fine cells, we avoid diffusing the interface thanks to Step ⑥.

Complex though Figure 2 may seem, it corresponds to a standard resolution of an advection equation on different grids (Steps 1 and 1'). Following steps are communications between those grids and consist of interpolations, operations on vectors and selection of more adapted grids. Results are exactly the same as those obtained with a global refinement, except for the fact that we improve efficiency by reducing computational costs. This is a consequence of the control of diffusion thanks to the Després-Lagoutière scheme: the interface is captured precisely and thus embedded into the fine grid. That would not be the case with the upwind scheme for instance. The coarse solutions $Y^n_{G_0}$ provide a prediction of how the discontinuity may move whereas we use fine solutions $Y^n_{G_{1,n}}$ to compute more accurate values in regions of high activity.

3. Numerical results

We test here the AMR algorithm coupled with the Després-Lagoutière scheme on a 3D-advection equation (13) with initial condition shown on Figure 3(a) and with divergence-free velocity:

$$\boldsymbol{v}(t,x,y,z) = \cos\left(\frac{2\pi t}{T}\right)\begin{pmatrix} 2\sin^2(\pi x)\sin(2\pi y)\sin(2\pi z) \\ -\sin^2(\pi y)\sin(2\pi x)\sin(2\pi z) \\ -\sin^2(\pi z)\sin(2\pi x)\sin(2\pi y)\end{pmatrix}$$

in the domain $[0,1]^3$ (here $T=\frac{1}{6}$). The coarser grid G_0 has sizes $\Delta x=\Delta y=\Delta z=\frac{1}{64}$. We use just one level of refinement G_1. Since we set the refinement rate equal to 10, the finer grid size in all directions is $\frac{1}{640}$. We see on Figure 3(c) the moving patches matching the interface.

This is an interesting case to test the accuracy of an algorithm since after one period we should recover the initial condition. As in the 2D-case (see Ref. 15 for details on the prescribed velocity: Figs. 25-26), the thickness of the bubble becomes smaller than the grid size and this makes the bubble break (see Figure 3(e)).

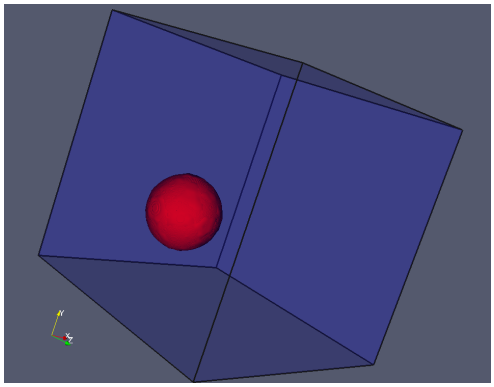

(a) Initial condition

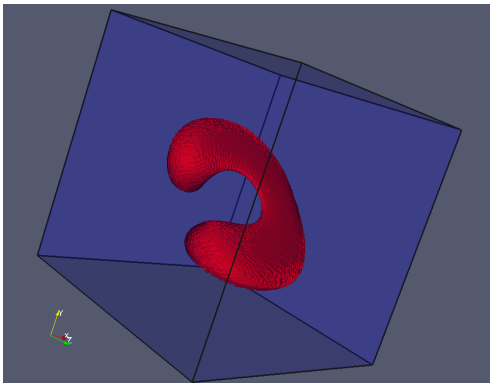

(b) Numerical solution at time $2min\ 11s$ (with AMR)

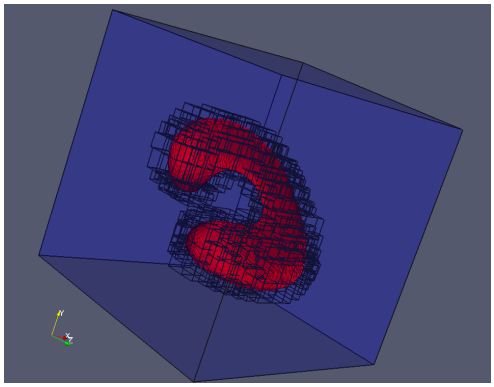

(c) Numerical solution at time $2min\ 11s$ with AMR patches

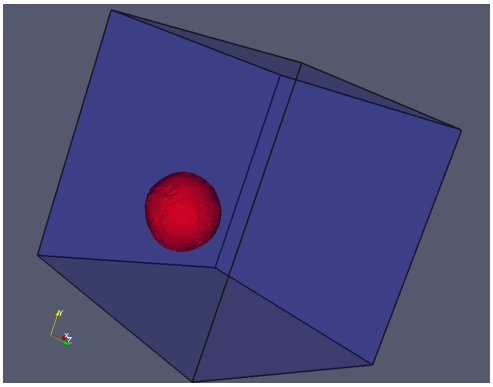

(d) Numerical solution at time $3min$ (with AMR)

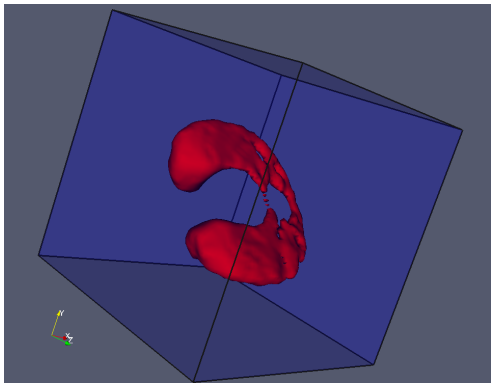

(e) Numerical solution at time $2min\ 11s$ (without AMR)

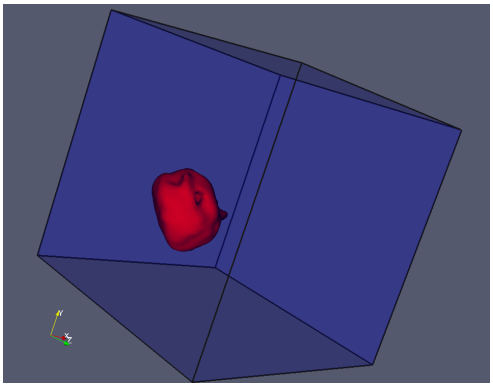

(f) Numerical solution at time $3min$ (without AMR)

Figure 3. Figures (a)–(d) show the deformation of a 3D-bubble due to a rotational periodic velocity field simulated with the described AMR-type method. As for Figures (e)–(f), there is no refinement.

This motivated our studies about improvements thanks to AMR. In this particular case, we see on Figure 3(d) the gain of AMR compared to the result on Figures 3(e)-(f). Looking at Figures 3(b) and 3(e) may suggest that this method avoids numerical mass loss and bubble breakings because of its accuracy in high activity regions, i.e. close to the interface where the solution shifts from 1 to 0. As regards efficiency, the algorithm is around fifty times faster than with a global refinement equivalent to the finest grid. We thus decrease drastically computational costs as well as use of memory.

B. LDC method for elliptic PDEs

We refer to the earlier works of Hackbush[11] and Anthonissen[1] for more details about Local Defect Correction Methods. Contrary to the latter authors, we use a staggered grid with nodes at centers of cells. We present here a simple application to the uncoupled Poisson-type PDE (11b)-(11d) assuming Y to be a datum. This assumption amounts to considering the standard system in a bounded open domain Ω:

$$\begin{cases} \Delta\phi \overset{\Omega}{=} f\,, \\ \nabla\phi\cdot\boldsymbol{n} \overset{\partial\Omega}{=} 0, \end{cases} \qquad \text{provided that } \int_\Omega f(t,\boldsymbol{x})\,d\boldsymbol{x} = 0. \tag{15}$$

The idea of the LDC method consists in an iterative process involving resolution on two different levels of grids. If we know that the solution of Eq. (15) has large variations[c] in a subset $\Omega_l \subset \Omega$, we construct:

- a coarse mesh G_0 with size $H > 0$. $(A_i)_{1\leqslant i\leqslant N}$ are the centers of G_0 cells, $\Omega^H = \{A_i,\ 1 \leqslant i \leqslant N\}$ and $\mathcal{A}^H = co(A_i)$ are respectively the set and convex hull of those nodes;
- a finer grid G_1 of size $h < H$. We note Ω_l^h and $\mathcal{A}_l^h$ the set and convex hull of G_1 vertices. Grid G_1 is such that $\Omega_l \subset \mathcal{A}_l^h$.

See Figure 4. We first solve:

$$\Delta^H \phi_0^H = f^H \tag{16}$$

on Ω^H where Δ^H is the standard five-point discretization.[d] The right-hand side in Eq. (16) takes into account the source term f and the Neumann BC. Once Eq. (16) solved, we consider the local problem on Ω_l^h imposing Dirichlet conditions $\phi_0^h = \mathbb{P}_h^H(\phi_0^H)$. The projection $\mathbb{P}_h^H$ corresponds to an interpolation at fine grid nodes located at the interface $\partial\mathcal{A}_l^h$ except at those potential ones belonging to adjacent cells to $\partial\Omega$: as $\partial G_1 \cap \partial\Omega$ might be nonempty, BC can be pure Dirichlet or mixed Dirichlet-Neumann type (see Figure 4 for an example). If a node belongs to a cell that is simultaneously adjacent to the physical boundary $\partial G_1 \cap \partial\Omega$ and to the inner one $\partial(G_0 \backslash G_1)$, we can impose either Dirichlet or Neumann BC. In all cases, the problem:

$$\Delta^h \phi_0^h = f^h \tag{17}$$

is well-posed, using a five-point stencil for Δ^h. Given ϕ_0^h, we now go back to the coarse problem solving:

$$\Delta^H \phi_1^H = f^H + d_{l,0}^H. \tag{18}$$

In Eq. (18), the perturbation $d_{l,0}^H$ is the residual on $\Omega^H \cap \mathcal{A}_l^h$. More precisely, we correct locally the discretization error with ϕ_0^H by means of the more accurate solution ϕ_0^h. We iterate the process, alternating corrected Neumann problems (18) and updated Dirichlet (or mixed Neumann-Dirichlet) problems (17).

IV. Numerical results

We combine in this last section the two algorithms developped above for hyperbolic and elliptic equations in order to solve the ABV model (11).

The 2D-example that we treat here corresponds to the initial condition on Figure 5(a), i.e. $\Omega = [-1,1]^2$ and $\Omega_1(0)$ is the union of two disjoint circles. We set $\psi \equiv 1$ in Eq. (11b) that corresponds to a uniform dilatation and we discretize Ω with a 100×100 grid. Refinement rate in patches is equal to 6.

[c] In our particular case, Ω_l is determined during the hyperbolic step of the algorithm.

[d] On the coarse grid, the Neumann problem (15) is ill-posed. The operator Δ^H is solved with a modified Conjugated Gradient method forcing the solution to stay in the zero mean-value function space.

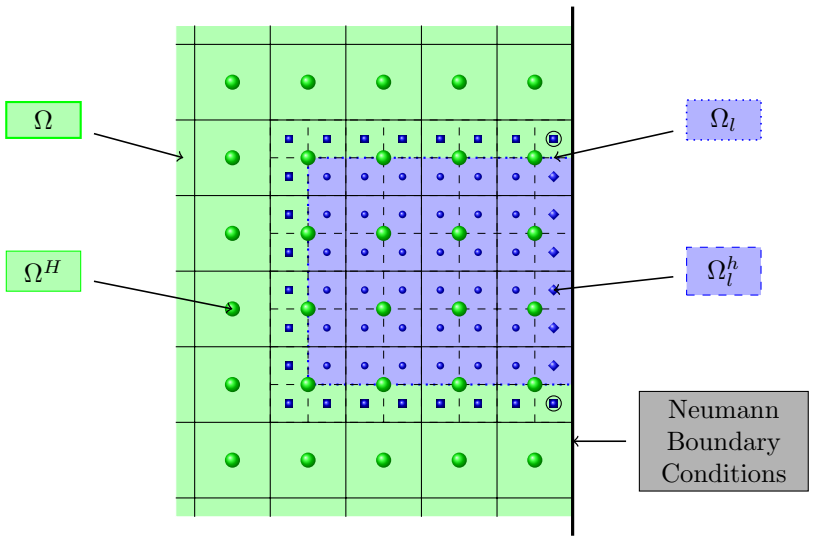

Figure 4. Example of LDC-type grids with $h = H/2$. Larger circle nodes belong to the coarser grid G_0 whereas grid G_1 consists of blue nodes (squares, diamonds and small balls). Squares correspond to Dirichlet boundary, diamonds to Neumann boundary and balls to inner points. Circled squares can be applied either BC.

There is an obvious numerical gain applying our algorithm. Indeed, as coalescence is not supported by our model at the continuous level, Figure 5(d) shows that results obtained without the techniques described above are not coherent with our model. With higher resolution, we check that interfaces remain intact and that there is no coalescence (Figures 5(a)–(c)). Those results make us think that increase in accuracy enables to recover physical properties. Morever, as showed in Figure 5(e), our method provides a perfect matching between exact and computed volumes, while without AMR, volume increases more slowly than it should do. Exact volume is computed by means of Formula (12). Here the function ψ is constant and we notice that the volume computation in the case without AMR worsens when we choose ψ with larger variations.

We finally notice that even if the two interfaces are initially recovered by disjoint patches, they are getting so close that single patches are enough to capture them.

V. Conclusion

We have presented the combination between three algorithms so as to solve a system of coupled hyperbolic-elliptic partial differential equations. We apply the Després-Lagoutière scheme to handle the advection equation, an AMR-type technique to improve the accuracy in the resolution of the latter equation, and finally a LDC-type method to treat the Laplace equation. Finer grids are used to adapt to the current solution variations, especially to capture interfaces in bubble modeling. Numerical simulations emphasize both performance and relevance of our method due to an increased accuracy, a faster resolution and savings in memory. Morever, we can readily contemplate parallelization in order to obtain faster results due to the structure of our code.

However, the system of PDEs we simulated here is derived from more physical systems. As our algorithm accurately simulates the Abstract Bubble Vibration model, it may turn out to be useful to study the potential-DLMN system which consists of a temperature evolution equation and a similar system to the studied ABV model with more complex coupling. Further studies will involve the global DLMN system with the non zero free-divergence part of the velocity field.

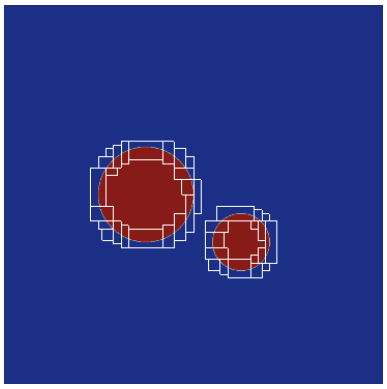

(a) Initial condition

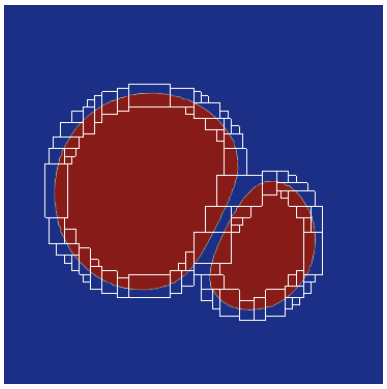

(b) Numerical solution at time $2s$ with AMR-LDC

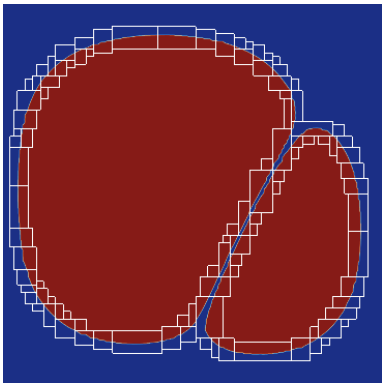

(c) Numerical solution at time $3s$ with AMR-LDC

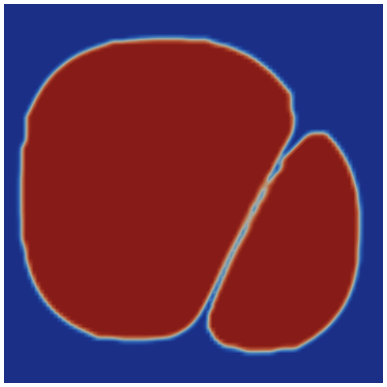

(d) Numerical solution at time $3s$ without AMR-LDC

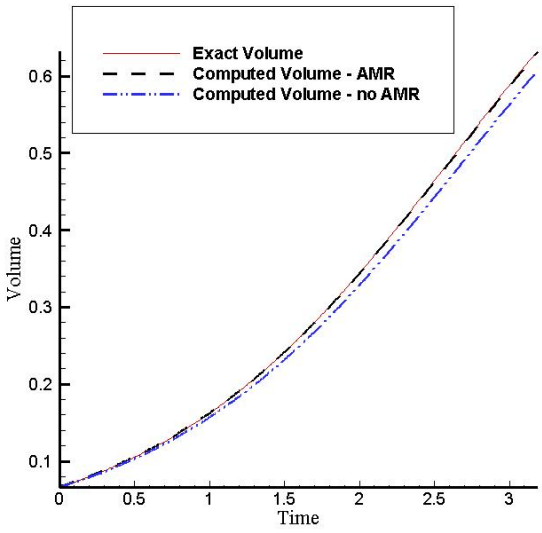

(e) Volumes

Figure 5. Figures (a)–(c) show the evolution of two bubbles governed by the ABV model with AMR-LDC. Figure (d) is obtained without any refinement technique. Figure (e) shows a comparison between exact and computed volumes with and without AMR.

References

[1]M. Anthonissen. *Local Defect Correction Techniques: Analysis and Application to Combustion*. PhD thesis, Eindhoven University of Technology, 2001.

[2]M. Berger and P. Colella. Local adaptive mesh refinement for shock hydrodynamics. *Journal of Computational Physics*, 82(1):64–84, 1989.

[3]M. Berger and J. Oliger. Adaptive methods for hyperbolic partial differential equations. *Journal of Computational Physics*, 53:484–512, 1984.

[4]M. Berger and I. Rigoutsos. An Algorithm for Point Clustrering and Grid Generation. *IEEE Transactions in Systems, Man, and Cybernetics*, 21(5):1278–1286, 1991.

[5]R. Courant and D. Hilbert. Methods of Mathematical Physics. *New York*, 1, 1953.

[6]S. Dellacherie. On a diphasic low mach number system. *ESAIM: M2AN*, 39(3):487–514, 2005.

[7]S. Dellacherie. Numerical resolution of a potential diphasic low Mach number system. *Journal of Computational Physics*, 223(1):151–187, 2007.

[8]S. Dellacherie and O. Lafitte. Existence et unicité d'une solution classique à un modèle abstrait de vibration de bulles de type hyperbolique - elliptique. *Publication du Centre de Recherches Mathématiques de Montréal (Canada), CRM-3200*, 2005.

[9]B. Després and F. Lagoutière. Contact Discontinuity Capturing Schemes for Linear Advection and Compressible Gas Dynamics. *Journal of Scientific Computing*, 16(4):479–524, 2001.

[10]P. Embid. Well-posedness of the nonlinear equations for zero Mach number combustion. *Comm. in Partial Differential Equations*, 12(11):1227–1283, 1987.

[11]W. Hackbush. Local defect correction and domain decomposition techniques. *Defect Correction Methods. Theory and Applications, Computing*, 5:89–113, 1984.

[12]J.-C. Jouhaud. *Méthode d'Adaptation de Maillages Structurés par Enrichissement*. PhD thesis, Bordeaux University, 1997.

[13]F. Lagoutière. *Modélisation mathématique et résolution numérique de problèmes de fluides à plusieurs constituants*. PhD thesis, Paris-6 University, 2000.

[14]J. Quirk. *An Adaptive Grid Algorithm for Computational Shock Hydrodynamics*. PhD thesis, College of Aeronautics, Cranfield University, Bedford, UK, 1991.

[15]W.J. Rider and D.B. Kothe. Reconstructing volume tracking. *Journal of Computational Physics*, 141(2):112–152, 1998.

[16]J. Ryan and M. Borrel. Adaptive Mesh Refinement: a coupling Framework for Direct Numerical Simulation of reacting Gas Flow. *Inst. of Comp. Fluid Dynamics*, 2004.